RESEARCH PAPER

Confined/Unconfined Crystallization of Poly (3-hexylthiophene) in Melt/Solution Environments containing Carbonic Materials and Correlated Thermal and Structural Behaviors

S. Agbolaghi

* *s.agbolaghi@azaruniv.ac.ir*

Received: July 2019 Revised: December 2019 Accepted: January 2020

Chemical Engineering Department, Faculty of Engineering, Azarbaijan Shahid Madani University, Tabriz, Iran.

DOI: 10.22068/ijmse.17.2.39

Abstract: *Confined and unconfined crystallization of poly (3-hexylthiophene) (P3HT) were studied in the solution-grown supramolecules and melt-grown systems using a differential scanning calorimeter. The carbon nanotube (CNT), reduced graphene oxide (rGO), their functionalized (CNT-f-COOTh and rGO-f-TAA), and grafted (CNT-g-PDDT and rGO-g-PDDT) derivatives were employed to develop the samples. The absorbance, structure details via Scherrer formula, fusion enthalpy (ΔHm), and crystallinity (Xc) were measured in two distinct confined/unconfined crystallization environments. Although the functionalized-CNT/rGO precursors partially reduced the crystallite qualities concerning the pristine CNT and rGO ones in the solution-grown supramolecules, they did not affect the structural properties in the melt-grown samples. Grafted carbonic materials could be considered as appropriate seeds for the arrangement of P3HTs in both solutions and melt crystallization. The best absorbances, larger and more compact crystals, higher melting point, ΔHm, and Xc values were recorded for the pre-developed CNT-g-PDDT/P3HT stem-leaf (6.09–22.51 nm, 3.52–13.89 Å, 239.8 °C, 30.86 J/g and 83.40%) and rGO-g-PDDT/P3HT coarse-patched (5.96–20.76 nm, 3.57–13.95 Å, 237.6 °C, 29.13 J/g and 78.73%) supramolecules. Although the melt-grown CNT-g-PDDT/P3HT (201.4 °C, 215.3 °C, 16.22 J/g and 43.84%) and rGO-g-PDDT/P3HT (205.4 °C, 218.8 °C, 18.06 J/g and 48.81%) nanostructures were not as perfect as the respective solution-grown nano-hybrids, they were well-arranged for the CNT/P3HT, CNT-f-COOTh/P3HT, rGO/P3HT, and rGO-f-TAA/P3HT samples.*

Keywords: *Crystallization, P3HT, Supramolecule, Scherrer formula, Fusion enthalpy.*

1. INTRODUCTION

Poly (3-alkylthiophene)s (P3ATs) have become a model system for research on conjugated polymers in terms of both fundamental and application-oriented studies [1]. In particular, the regioregular poly (3-hexylthiophene) (RR-P3HT) has been amply studied because of excellent electrical properties, great solubility, and processability [2–5]. For interpreting the functional behavior of conjugated crystalline structures, it is necessary to unravel the relationship between the thermal and optical properties and nano/microstructures [6–8]. Balko et al. [9] estimated the crystallinity of P3HT crystals and measured the fusion enthalpy of ΔH°m = 33 J/g for a perfect P3HT crystal. Snyder et al. [10] included finite crystal size effects in their calculations for the P3HT crystals having different thicknesses and molecular weights. Extrapolating the heat of fusion divided by the crystallinity to the infinite lamellar thickness led to ΔH°m = 49 J/g for a perfect crystal. Lee and Dadmun [11] determined the fusion enthalpy as a function of density for their P3HT samples. Knowing the density of a perfect P3HT crystal from the unit cell structure, extrapolation of the fusion heat to this density yielded ΔH°m in the range of 37–50 J/g.

The conjugated polymers such as polypyrroles [12], polyanilines [13], poly (3alkylthiophene) [14], poly (phenylene vinylenes) [15] and poly (arylene ethynylene) [16] have also depicted efficient decorations on carbon nanotubes (CNTs). The optoelectronic and conductivity properties of P3HT depend on the head-to-tail regioregularity; the higher regioregularity, the higher conductivity [17–19]. The P3HT can self-assemble through solution crystallization in the presence of CNTs into hierarchical supramolecular structures, in which P3HT chains grow into nanowires with the stacking direction perpendicular to the CNT axis [20–23]. The rigid P3HTchains

in the solution can be adsorbed on CNTs via strong π-interactions [24]. The epitaxial growth of P3HT nanofibrils on CNTs was also reported [25]. Based on differential scanning calorimetric (DSC) analyses, Dias and coworkers [23] reported a significant increase in polymer crystallinity in the carbon nanotube composites. The crystallization kinetics of high-density and low-density polyethylenes on CNTs was also investigated by Depan and coworkers [26]. DSC-based thermal examination indicated that the CNTs can provide the nucleation sites for polyethylene to accelerate the crystal growth rate. The induced crystallization of P3ATs onto the graphenic materials was also vastly reported [27–33], such as well-oriented ultrathin P3HT films on graphene [30], graphene oxide (GO)/P3AT mixture having semi-spherulites [32], connecting the individual reduced graphene oxide (rGO) monolayers with P3HT nanowires [27], etc.

Herein, the crystallization of P3HT was investigated in pre-developed supramolecules based on the CNT and rGO and their functionalized and grafted derivatives as well as DSC-crystallized nanostructures. The absorbance, structure details via Scherrer formula, melting enthalpy (ΔHm) and crystallinity (Xc) were focused in two different crystallization environments. The impact of functionalization and grafting of nucleating agents was studied on ordering and sample characteristics and the results were compared with the features of pristine P3HT crystals.

2. EXPERIMENTAL

The regioregular P3HT (RR-P3HT, > 99%) with the molecular weight (Mn) of 30 kDa and the dispersity of 1.18 was synthesized through Grignard metathesis polymerization [34]. FT-IR and 1HNMR spectra, as well as the GPC chromatogram, are reported in Fig. S1. The functionalization of CNTs was carried out with an oxidation method with sonication of sulfuric acid (97 %):nitric acid (65 %) with a ratio of 1:3 v/v for 6 h at 50 °C. The 2-hydroxymethyl thiophene (CNT-COOH-f-HMTh) macroinitiator was synthesized by esterification of CNT-COOH with 2-hydroxymethyl thiophene using p-TSA as a dehydrating agent (5 wt% of acid) at 140 °C for 6 h. In a forward step, a reactor was charged with CNTs-COOH-f-HMTh and dried CHCl3 and then sonicated for 1 h to reach a homogeneous suspension. The 3-dodecylthiophene monomer was then added and the reaction mixture was deaerated by bubbling highly pure argon for 5 min. In a parallel system, the anhydrous ferric chloride was dissolved in dried acetonitrile and slowly added to the reaction mixture at a rate of 5 ml min^{-1}. The reaction mixture was refluxed for 1 day at 25 °C under an inert atmosphere. The reaction was terminated by pouring the flask content into methanol. The solution was filtered, precipitated, and dried to reach a dark color powder. The chemical structures of pure CNT, CNT-COOH, CNT-f-COOTh, and CNT-g-PDDT are depicted in Fig. S2(a). The FT-IR spectrum of CNT, CNT-COOH, and thiophene functionalized/grafted CNTs are reported in Fig. S2(b). In the FT-IR spectrum of CNT-COOH, the stretching vibration of C=O in carboxylic acid appeared at 1728 cm^{-1} and a peak centered at 3442 cm^{-1} was detected for the alcoholic/phenolic/carboxylic groups (Fig. S2(b)). In the FT-IR spectrum of CNT-f-COOTh, the vibrational peaks resulting from the stretching of C−S and C=O were detected at 715 and 1656 cm−1, respectively. The most important bands in FT-IR spectrum of CNT-g-PDDT were the weak aromatic α and β hydrogens of thiophene rings at 3000−3100 cm^{-1}, γ(C–H) in the aromatic ring at 719 cm^{-1}, the aromatic C=C stretching vibration at 1423, 1512 cm^{-1} and C−S stretching vibration in thiophene rings at 702 cm^{-1}. Further vibration from the CH-aliphatic bonds was also detected at 2800−2950 cm^{-1}. After graft polymerization onto the CNT-f-COOTh, the intensity of bands related to the polythiophene derivatives increased, instead, the intensity of peaks attributed to CNTs decreased due to their low concentration in the grafted sample.

Likewise, the rGO-f-TAA (Fig. S3(b)) was synthesized by the esterification of rGO (Fig. S3(a)) with 2-thiophene acetic acid in the presence of p-toluenesulfonic acid (p-TSA) at 140 °C within 6 h. FT-IR spectra of rGO-f-TAA are reported in Fig. S3(d). In a forward step, a reactor was charged with rGO-f-TAA and dried $CHCl_3$, and then was sonicated for 40 min to produce a homogeneous suspension. Hereafter, the synthesized 3-dodecylthiophene

monomer was added and the reaction mixture was bubbled for 15 min. In a separate system, the anhydrous ferric chloride was dissolved in dried acetonitrile. This solution was deaerated for 15 min, and then added to the reaction mixture at a rate of 5 ml min^{-1}. The reaction mixture was refluxed for 1 day at room temperature under an inert atmosphere. The polymer solution was filtered, precipitated into excess methanol, and dried in reduced pressure to give a dark powder (Fig. S3(c)). FT-IR spectra of synthesized rGO-g-PDDT are represented in Fig. S3(d). The successful synthesis of rGO-f-TAA was verified by the appearance of new bands like the stretching vibrations of aliphatic and aromatic C–H at 3050–2800 cm^{-1}, γ(C–H) in the aromatic ring at 669 and 783 cm^{-1}, unreacted hydroxyl end groups as a band centered at 3427 cm^{-1}, and the aromatic C=C stretching vibration at 1546 cm^{-1}. Moreover, the peak at 1662 cm^{-1} may be attributed to the carbonyl stretching vibration of 2-thiopheneacetate groups (Fig. S3(d)). The most important bands in FT-IR spectrum of rGO-g-PDDT consisted the aromatic α and β hydrogens of thiophene rings at 3000–3050 cm^{-1} region, γ(C–H) in the aromatic ring at 775 cm^{-1}, the aromatic C=C stretching vibration at 1423 cm^{-1}, and C–S stretching vibration at 678 cm^{-1} in thiophene rings. The successful grafting of PDDT onto functionalized nanosheets was verified by the appearance of new bands such as stretching vibration of the carbonyl group at 1710 cm^{-1}, C–O stretching vibrations at 1209 cm^{-1}, and the stretching vibrations of aliphatic and aromatic C–H at 2800–3050 cm^{-1}.

To prepare the pre-designed supramolecules, the CNT, rGO, and functionalized and grafted precursors (CNT-f-COOTh, rGO-f-TAA, CNT-g-PDDT, and rGO-g-PDDT) were dispersed in dimethyformamide (DMF) and subjected to stirring and sonication. The P3HT was dissolved in toluene and added to the vial containing sonicated CNT, rGO, CNT-f-COOTh, rGO-f-TAA, CNT-g-PDDT and rGO-g-PDDT samples in DMF and purged with high purity nitrogen and the dissolution and stirring steps were then performed. The ratio of polymer to carbonic material was fixed at 10:1 and the concentration was 0.1 wt%. A primary dissolution was conducted at 100 °C for 1 h. The resulted vials were transferred to the sonication step at 50 °C for 8 h and also to the crystallization step at 30 °C for 1 day. Moreover, the P3HT nanofibers were grown in toluene and using the isothermal crystallization method. The solution with 0.1 wt% concentration was homogenized for 1 h at 100 °C in toluene. The vial was then switched to the crystallization temperature of 30 °C in a Lauda Alpha RA8 circulator and kept for 1 day. The prepared samples were then filtered and analyzed and also put into DSC pans for thermal recordings.

The DSC-grown crystals were prepared using a TA Q20 calorimeter system under flowing nitrogen gas. For isothermal crystallization, 4 mg of the P3HT, P3HT:CNT, P3HT:rGO, P3HT:CNT-f-COOTh, P3HT:rGO-f-TAA, P3HT:CNT-g-PDDT and P3HT:rGO-g-PDDT were put into a DSC pan. The weight ratios were 10:1 for the polymer:carbonic material. The pan was sealed and heated up to 250 °C with a heating rate of 20 °C min^{-1} and kept at this temperature for 1 min for completion of the melting process. The temperature was then decreased to 30 °C with 100 °C min^{-1} and remained at this temperature for 1 day. The temperature was then escalated with a rate of 20 °C min^{-1} to detect the melting temperature (Tm) and the area under this peak as the fusion enthalpy (ΔHm).

3. RESULTS AND DISCUSSION

In the current work, the solution- and melt-grown nanostructures fabricated based on the RR-P3HT as well as CNT, CNT-f-COOTh, CNT-g-PDDT, rGO, rGO-f-TAA and rGO-g-PDDT precursors were investigated from the structural, thermal, and optical viewpoints. The prepared samples were characterized by transmission electron microscope (Philips CM30 TEM). Fig. 1(a) depicts a TEM image of homo-P3HT nanofibrils grown in toluene at 30 °C within 1 day. The diameters of P3HT crystalline nanofibers ranged in 10−15 nm. Similar nanofibrils were also grown in the presence of CNT and rGO seeds. The CNT/P3HT and rGO/P3HT nano-hybrids are represented in Figs. 1(b) and (c), respectively. In the CNT/P3HT and rGO/P3HT supramolecules, the P3HT fibrillar crystals were grown from the carbonic material's surface. When the pristine CNTs and rGO nanosheets were used to prepare the supramolecules, the RR-P3HT chains interacted with their thiophenic rings with

the surface of carbonic materials. The primarily attached P3HT chains acted as nucleation agents for the next P3HTs, thereby the P3HT nanofibers were developed with π-stacking. In similar growth conditions and only via functionalization of the surfaces of CNT and rGO (CNT-f-COOTh and rGO-f-TAA), the configurations of nano-hybrids were significantly altered. The shish-kebab nanostructures composed of functionalized-CNT shish and P3HT crystalline kebabs were developed using the CNT-f-COOTh and RR-P3HT backbones. Fig. 1(d) shows a typical shish-kebab CNT-f-COOTh/P3HT supramolecule. This configuration was originated from the strong interactions between the hexyl side chains of RR-P3HT chains and −COOTh functionalities of CNTs. The morphology acquired for the rGO-f-TAA/P3HT nano-hybrids was a delicate-patterned nanosheet composed of P3HT nano-crystals (Fig. 1(e)). When the surfaces of CNTs were grafted with the thiophenic oligomers of PDDT, the stem-leaf configurations fabricated from the grafted-CNT stems and RR-P3HT leaves were detected. A typical CNT-g-PDDT/P3HT stem-leaf supramolecule is illustrated in Fig. 1(f). In the stem-leaf nanostructures, the P3HT grafts onto the CNT surface may assist the host RR-P3HT backbones to attach perpendicularly to the CNT. The surface of grafted-rGO with PDDT (rGO-g-PDDT) was patterned by the coarse rectangular patches (Fig. 1(g)). The darker surface areas belonged to the ordered P3HTs, owing to different electron densities of P3HT and rGO. On the other hand, the nanostructures composed of

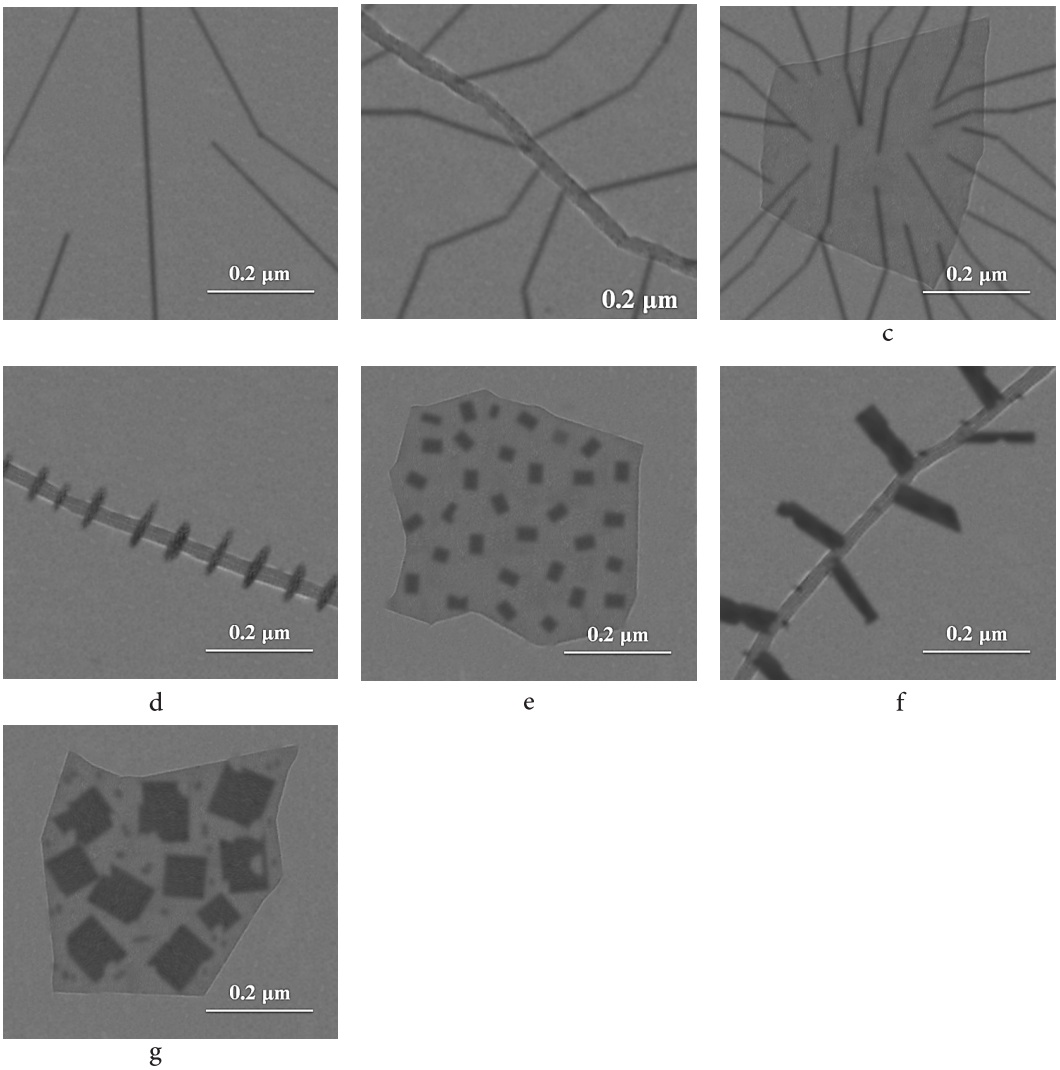

Fig. 1. TEM bright images of pristine P3HT crystals (a); CNT/P3HT (b); rGO/P3HT (c); CNT-f-COOTh/P3HT (d); rGO-f-TAA/P3HT (e); CNT-g-PDDT/P3HT (f); rGO-g-PDDT/P3HT (g).

similar constituents were prepared inside the DSC pans as the confined growth environments.

The ultraviolet-visible (UV-Vis) absorption spectra were recorded on a Lambda 750 UV-Vis spectrometer using the thin films. UV-Vis spectra of distinct samples subsuming P3HT, CNT/P3HT, rGO/P3HT, CNT-f-COOTh/P3HT, rGO-f-TAA/P3HT, CNT-g-PDDT/P3HT and rGO-g-PDDT/P3HT nanostructures developed in dilute solutions and DSC pans are represented in Figs. 2(a) and (b), respectively. The best absorbances were recorded for the pre-developed CNT-g-PDDT/P3HT and rGO-g-PDDT/P3HT supramolecules. Compared with the pre-developed and DSC-grown P3HT nano-crystals having only the principal peaks at 478 (Fig. 2(a)) and 444 nm (Fig. 2(b)), respectively, A_{0-2}, A_{0-1}, and A_{0-0} identifying peaks were detected at 462, 562, and 638 nm for the CNT-g-PDDT/P3HT stem-leaf supramolecules and 456, 550, and 637 nm for the rGO-g-PDDT/P3HT coarse-patched nano-hybrids (Fig. 2(a)). The corresponding melt-grown CNT-g-PDDT/P3HT and rGO-g-PDDT/P3HT samples demonstrated the identifying peaks of (438, 528, and 606 nm) and (450, 534, and 608 nm), respectively (Fig. 2(b)). By large, the P3HT nanofibrils and supramolecules represented better optical properties in the pre-developed state with respect to the melt-grown state including more red-shifted and more intensified peaks. This phenomenon was also detected in the CNT/P3HT, rGO/P3HT, CNT-f-COOTh/P3HT, and rGO-f-TAA/P3HT samples. The A_{0-2}, A_{0-1}, and A_{0-0} identifying peaks were recorded at (450, 550, and 594 nm), (442, 545, and 575 nm), (450, 544, and 581 nm) and (450, 543, and 582 nm) for the CNT/P3HT, rGO/P3HT, CNT-f-COOTh/P3HT, and rGO-f-TAA/P3HT nano-hybrid films, respectively. However, the corresponding peak groups were (402, 532, and 589 nm), (418, 530, and 570 nm), (406, 531, and 588 nm), and (418, 527, and 566 nm) for the DSC-crystallized systems. Although the CNT-based supramolecules represented better absorbances than the rGO-based ones, in the DSC pans the rGO nanosheets were better seeds for the crystallization of P3HTs. Also, the functionalization of CNT and rGO precursors did not significantly affect the optical properties.

The structural details on the pre-designed and melt-grown nanostructures were acquired through the XRD measurements (CMOS flat panel X-ray detector (C9728DK)). The dimensions of P3HT crystallites within the crystals were monitored by the full width half maximum (FWHM, ΔQ) of (100) and (020) peaks based on the Scherrer equation, i.e., $D = \frac{2\pi}{\Delta Q}$ [35,36]. Furthermore, the layer spacings between the crystallographic planes were determined with (100) and (020) Bragg peak positions [37]. The XRD patterns of P3HT, CNT/P3HT, rGO/P3HT, CNT-f-COOTh/

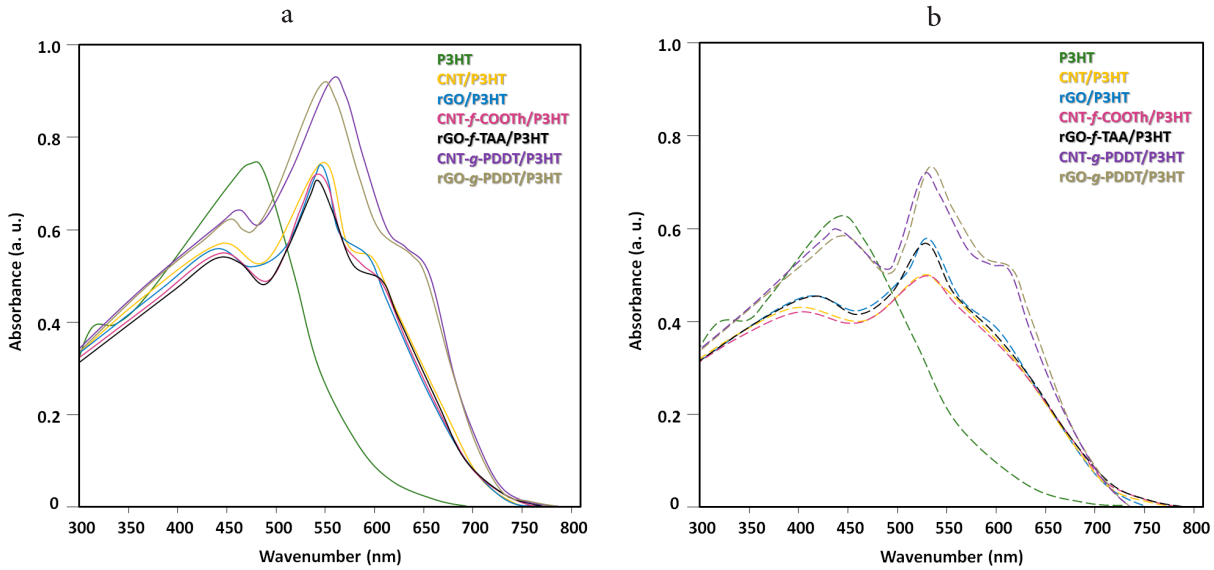

Fig. 2. UV-Vis spectra of P3HT, CNT/P3HT, rGO/P3HT, CNT-f-COOTh/P3HT, rGO-f-TAA/P3HT, CNT-g-PDDT/P3HT and rGO-g-PDDT/P3HT nanostructure thin films in pre-developed (a) and DSC-crystallized (b) states.

P3HT, rGO-f-TAA/P3HT, CNT-g-PDDT/P3HT and rGO-g-PDDT/P3HT nanostructures in the solution- (filled lines) and melt-grown (dashed lines) states are reported in Fig. 3. The (100) and (020) growth prisms were recorded at 0.441 and 1.657 $Å^{-1}$ for the solution-grown P3HT nanofibrils and 0.439 and 1.631 $Å^{-1}$ for the melt-grown samples. Based on XRD patterns reported in Fig. 3 and using the Scherrer formula and Bragg peak positions, the crystallite sizes and d-spacing values in the hexyl side chains direction were $D_{(100)}$ = 20.36 and 17.84 nm (Fig. 4(a)) and $d_{(100)}$ = 14.22 and 14.28 Å (Fig. 4(b)) for the solution- and melt-grown P3HT nano-crystals, respectively. Likewise, the crystallite sizes and d-spacing values in π-stacking direction were $D_{(020)}$ = 4.21 and 3.96 nm (Fig. 4(a)) and $d_{(020)}$ = 3.79 and 3.85 Å (Fig. 4(b)) for the former and latter P3HT nanostructures. The results demonstrated that the pre-designed P3HT nanofibrils possessed the larger crystallites with more ordered and packed structures with respect to the DSC-confined systems.

Via incorporation of CNT and rGO precursors as seeds into the crystallization environments, the crystallite sizes decreased and the d-spacing values increased in both hexyl side chains and π-stacking directions, demonstrating that the CNTs and rGO nanosheets were not capable of enhancing the crystallization qualities. The structural data for the pre-designed CNT/P3HT ($D_{(100)}$ = 17.11 nm, $D_{(020)}$ = 3.33 nm, $d_{(100)}$ = 14.33 Å and $d_{(020)}$ = 3.89 Å) and rGO/P3HT ($D_{(100)}$ = 16.82 nm, $D_{(020)}$ = 3.24 nm, $d_{(100)}$ = 14.36 Å and $d_{(020)}$ = 3.93 Å) supramolecules are represented in the bar graphs of Figs. 4(a) and (b). The seeding roles of CNT and rGO were more insignificant in the melt crystallization inside the DSC pans and the smallest and loosest crystallites were grown in the CNT/P3HT ($D_{(100)}$ = 14.69 nm, $D_{(020)}$ = 3.06 nm, $d_{(100)}$ = 14.61 Å and $d_{(020)}$ = 4.20 Å) and rGO/P3HT ($D_{(100)}$ = 14.91 nm, $D_{(020)}$ = 3.12 nm, $d_{(100)}$ =

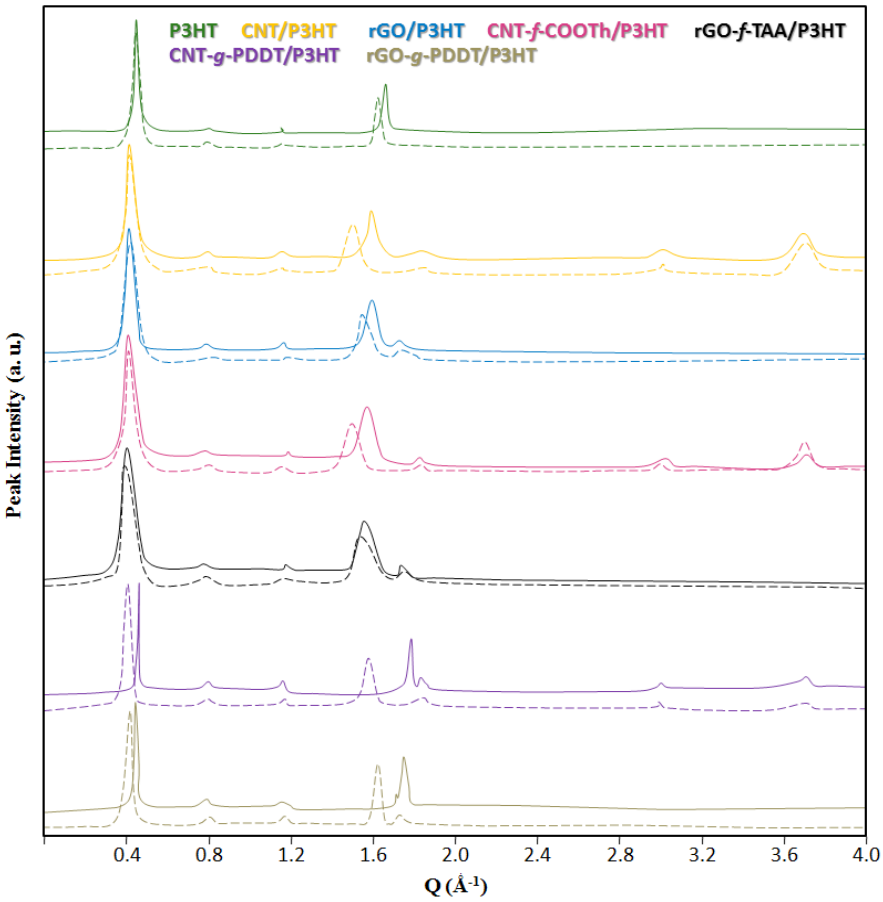

Fig. 3. XRD patterns of pure P3HT and the CNT/P3HT, rGO/P3HT, CNT-f-COOTh/P3HT, rGO-f-TAA/P3HT, CNT-g-PDDT/P3HT and rGO-g-PDDT/P3HT nanostructures prepared in dilute solutions (filled patterns) and DSC pans (dashed patterns).

14.51 Å and $d_{(020)}$ = 4.10 Å) systems.

Although the functionalized-CNT/rGO precursors, i.e., CNT-f-COOTh (16.37 nm, 3.15 nm, 14.39 Å, and 3.97 Å) and rGO-f-TAA (16.31 nm, 3.08 nm, 14.41 Å, and 3.99 Å) to some extent decreased the crystallite qualities compared to the pristine CNT (17.11 nm, 3.33 nm, 14.33 Å, and 3.89 Å) and rGO (16.82 nm, 3.24 nm, 14.36 Å, and 3.93 Å) ones in the solution-grown supramolecules, they did not affect the structural properties in the melt-grown samples. The structural characteristics of melt-grown CNT-f-COOTh/P3HT (14.70 nm, 3.05 nm, 14.62 Å and 4.19 Å), CNT/P3HT (14.69 nm, 3.06 nm, 14.61 Å and 4.20 Å), rGO-f-TAA/P3HT (14.90 nm, 3.12 nm, 14.52 Å and 4.09 Å) and rGO/P3HT (14.91 nm, 3.12 nm, 14.51 Å and 4.10 Å) nanostructures are reported in Fig. 3 and Figs. 4(a) and (b). In a large contrast, the grafted carbonic materials (CNT-g-PDDT and rGO-g-PDDT) acted as appropriate seeding agents for the arrangement of P3HT chains in both dilute solution and melt crystallization. The P3HT crystallites were 22.51 and 6.09 nm in the hexyl side chains and π-stacking directions, respectively, in the CNT-g-PDDT/P3HT stem-leaf supramolecules. In these systems, the $d_{(100)}$ and $d_{(020)}$ values were 13.89 and 3.52 Å, respectively. Similar results were reached for the rGO-g-PDDT/P3HT coarse-patched supramolecules, i.e., $D_{(100)}$ = 20.76 nm, $D_{(020)}$ = 5.96 nm, $d_{(100)}$ = 13.95 Å and $d_{(020)}$ = 3.57 Å. In fact, the stem-leaf supramolecules possessed the larger and more compact and ordered crystallites than the coarse-patched ones. The melt-grown CNT-g-PDDT/P3HT and rGO-g-PDDT/P3HT nanostructures did not represent the quality of corresponding stem-leaf and coarse-patched supramolecules; however, they had more suitable features compared with the melt-grown CNT-f-COOTh/P3HT, CNT/P3HT, rGO-f-TAA/P3HT and rGO/P3HT samples, i.e., $D_{(100)}$ = 17.01 nm versus 14.70 and 14.69 nm, $D_{(020)}$ = 3.28 nm versus 3.05 and 3.06 nm, $d_{(100)}$ = 14.34 Å versus 14.62 and 14.61 Å and $d_{(020)}$ = 3.93 Å versus 4.19 and 4.20 Å for the melt-grown CNT-g-PDDT/P3HT, CNT-f-COOTh/P3HT, and CNT/P3HT systems, respectively, and $D_{(100)}$ = 17.48 nm versus 14.90 and 14.91 nm, $D_{(020)}$ = 3.41 nm versus 3.12 and 3.12 nm, $d_{(100)}$ = 14.30 Å versus 14.52 and 14.51 Å and $d_{(020)}$ = 3.87 Å versus 4.09 and 4.10 Å for the melt-grown rGO-g-PDDT/P3HT, rGO-f-TAA/P3HT, and rGO/P3HT systems, respectively. The crystallite dimensions and d-spacings are reported in the bar graphs of Figs. 4(a) and (b). The peaks at 1.744 Å−1 with a d-spacing of 3.60 Å were attributed to the (002) plane of rGO. This peak was detected for the rGO/P3HT, rGO-f-TAA/P3HT, and rGO-g-PDDT/P3HT samples in both solutions and melt states (Fig. 3). Moreover, the peaks at 1.847, 2.990, and 3.694 Å−1 with the respective d-spacing values of $d_{(002)}$ = 3.40 Å, $d_{(100)}$ = 2.10 Å, and $d_{(004)}$ = 1.70 Å, were recorded because of the presence of CNT precursors in the CNT/P3HT, CNT-f-COOTh/P3HT, and CNT-g-PDDT/P3HT samples grown in both dilute solution and melt environments.

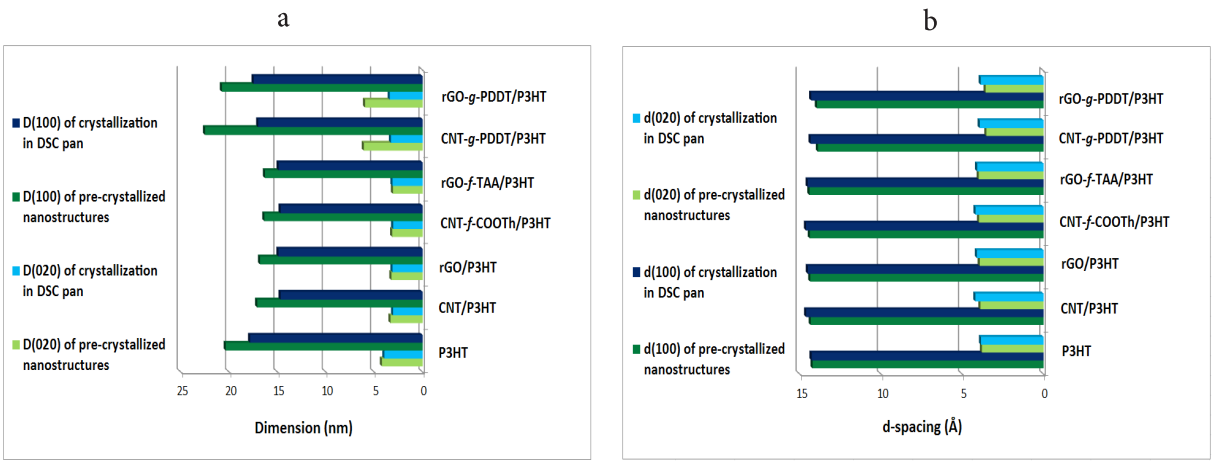

Fig. 4. Crystal sizes (a) and d-spacings (b) of pre-developed and DSC-crystallized nanostructures.

The thermal behaviors of pre-developed supramolecules and DSC-prepared nano-crystals, the melting endotherms, and crystallization exotherms were recorded using a TA Q20 calorimeter system. Fig. 5(a) exhibits the melting endotherms of P3HT, CNT/P3HT, rGO/P3HT, CNT-f-COOTh/P3HT, rGO-f-TAA/P3HT, CNT-g-PDDT/P3HT and rGO-g-PDDT/P3HT pre-designed supramolecules. A small peak detected at 53–58 °C represented destruction in the hexyl side chains ordering and at elevated temperatures (T_m), the P3HT backbone ordering was also ruined [38,39]. The crystallization exotherms and melting endotherms of the corresponding melt-grown nanostructures are also displayed in Fig. 5(b). The melting enthalpies or heat fusions (ΔH_m) were calculated from the area under the melting peaks. The crystallization percentages (X_c) were determined using the ideal melting enthalpy (37 J/g [11]). The pure P3HT nanofibers demonstrated the melting temperature (T_m) of 228.7 °C (Fig. 5(a) and Fig. 6), the fusion enthalpy (ΔH_m) of 20.14 J/g (Fig. 7), and the crystallinity of 54.43% (Fig. 8). In order to compare with the melt-grown P3HT crystals, the P3HT-filled DSC pan represented the T_c and T_m values of 206.8 and 219.3 °C, respectively (Fig. 5(b) and Fig. 6). In addition to the lower Tm, the ΔH_m and X_c values were also reduced in the melt-grown P3HT crystals (ΔH_m = 18.70 J/g (Fig. 7) and X_c = 50.54% (Fig. 8)). The solution-grown P3HT nanofibers had larger crystallites (20.36 nm versus 17.84 nm and 4.21 nm and 3.96 nm) with more packed structures (14.22 Å versus 14.28 Å and 3.79 Å versus 3.85 Å) and higher crystallinity (54.43% versus 50.54%).

The thermal and structural characteristics of CNT/P3HT and rGO/P3HT supramolecules were plummeted compared with the pure P3HT nano-crystals. As reported in Fig. 5(a), Fig. 6, Fig. 7 and Fig. 8, the T_m, ΔH_m, and X_c values were equal to (216.5 °C, 14.42 J/g and 38.97%) and (214.3 °C, 13.85 J/g and 37.43%) for the CNT/P3HT and rGO/P3HT pre-developed supramolecules. This could be originated from the smaller and looser-packed crystallites in the CNT/P3HT and rGO/P3HT supramolecules, i.e., 17.11 and 16.82 nm versus 20.36 nm in the hexyl side chains direction and 3.33 and 3.24 nm versus 4.21 nm in

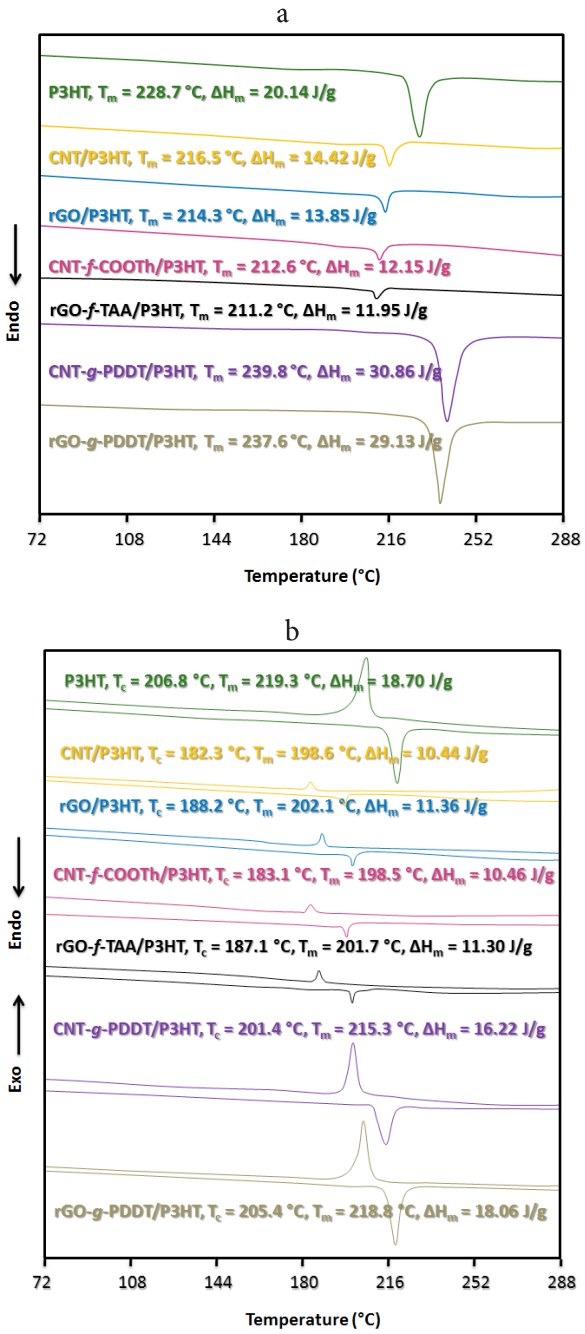

Fig. 5. (a) Melting endotherms of P3HT, CNT/P3HT, rGO/P3HT, CNT-f-COOTh/P3HT, rGO-f-TAA/P3HT, CNT-g-PDDT/P3HT and rGO-g-PDDT/P3HT pre-designed nano-hybrids; (b) crystallization exotherms and melting endotherms of corresponding DSC-crystallized nanostructures.

π-stacking direction; 14.33 and 14.36 Å versus 14.22 Å in the hexyl side chains direction and 3.89 and 3.93 Å versus 3.79 Å in π-stacking direction. The melt-grown CNT/P3HT and rGO/

P3HT nanostructures demonstrated further loose-packed and small crystallites. The constructing crystallites of solution-grown supramolecules encountered a higher opportunity for being arranged in more-ordered configurations. On the other side, in the confined melt environment, the crystallites were smaller and looser because of encountering a worse growth condition and bombarding the growing crystallites with the P3HT chains. Figs. 5–8 reports that the T_m, T_c, ΔH_m, and X_c values were (198.6 °C, 182.3 °C, 10.44 J/g and 28.22%) and (202.1 °C, 188.2 °C, 11.36 J/g and 30.70%) for the melt-grown CNT/P3HT and rGO/P3HT samples. The rGO nanosheets acted their seeding roles somehow better than very long CNTs.

The quality of grown crystallites in the CNT-f-COOTh/P3HT (212.6 °C, 12.15 J/g and 32.84%) and rGO-f-TAA/P3HT (211.2 °C, 11.95 J/g and 32.30%) supramolecules was less than those mounted onto the CNT/P3HT (216.5 °C, 14.42 J/g and 38.97%) and rGO/P3HT (214.3 °C, 13.85 J/g and 37.43%) nano-hybrids. On the contrary, in the melt-grown nanostructures, there were no differences between the unmodified and functionalized carbonic materials in playing the seeding role for the crystallization of P3HT backbones. Figs. 6–8 compare the T_m, Tc, ΔH_m and X_c data recorded for the DSC-prepared CNT-f-COOTh/P3HT (198.5 °C, 183.1 °C, 10.46 J/g and 28.27%), rGO-f-TAA/P3HT (201.7 °C, 187.1 °C, 11.30 J/g and 30.54%), CNT/P3HT (198.6 °C, 182.3 °C, 10.44 J/g and 28.22%) and rGO/P3HT (202.1 °C, 188.2 °C, 11.36 J/g and 30.70%) systems. Notably, the –COOTh and –TAA functionalities did not affect the crystallization procedure of host P3HTs in the confined growth environments.

In a forward step, the perfect CNT-g-PDDT/P3HT and rGO-g-PDDT/P3HT supramolecules were thermally analyzed. The highest melting point, fusion enthalpy, and crystallinity contents were recorded for the stem-leaf (Fig. 1(f)) and coarse-patched (Fig. 1(g)) nano-hybrids, as displayed in the endotherms of Fig. 5(a) and bar graphs of Figs. 6–8. The T_m, ΔH_m, and X_c data of (239.8 °C, 30.86 J/g and 83.40%) and (237.6 °C, 29.13 J/g and 78.73%) were obtained for the CNT-g-PDDT/P3HT stem-leaf and rGO-g-PDDT/P3HT coarse-patched supramolecules, respectively. The DSC-grown nanostructures composed of similar constituents (CNT-g-PDDT and rGO-g-PDDT, and P3HT host chains) did not represent similar thermal properties. The DSC pans were not suitable places for the supramolecular growth, and thus the Tm, ΔH_m, and X_c values conspicuously decreased. The T_c, T_m, ΔH_m, and X_c data were (201.4 °C, 215.3 °C, 16.22 J/g and 43.84%) and (205.4 °C, 218.8 °C, 18.06 J/g and 48.81%) for the melt-grown CNT-g-PDDT/P3HT and rGO-g-PDDT/P3HT nanostructures. Although the melt-grown CNT-g-PDDT/P3HT and rGO-g-PDDT/P3HT nanostructures were not as perfect as the corresponding solution-grown supramolecules, they were well-structured compared to the CNT/P3HT, CNT-f-COOTh/P3HT, rGO/P3HT, and rGO-f-TAA/P3HT systems.

The XRD and DSC measurements demonstrated that the grafted rGO nanosheets were the best seeding agents for the crystallization of P3HT chains in the melt state. The largest (D(100) = 17.48 nm and $D_{(020)}$ = 3.41 nm) and most-packed (d(100) = 14.30 Å and d(020) = 3.87 Å) crystallites and also the highest crystallinity (Xc = 48.81%) were acquired for the rGO-g-PDDT based melt-grown nanostructures. In both CNT and rGO precursors, the PDDT grafts assisted the crystallization and ordering of the host P3HT backbones in either dilute solution or melt state, thereby all-optical (Fig. 2), structural (Fig. 3), and thermal (Fig. 5) characteristics were progressed.

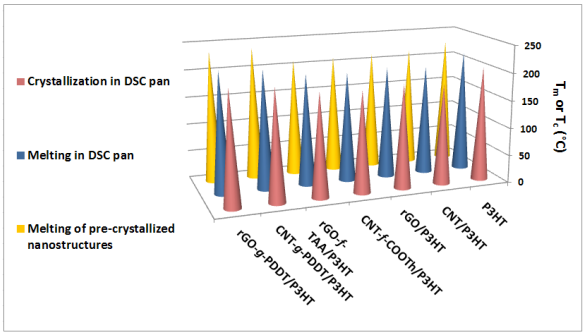

Fig. 6. Crystallization and melting temperatures of DSC-crystallized and pre-designed P3HT, CNT/P3HT, rGO/P3HT, CNT-f-COOTh/P3HT, rGO-f-TAA/P3HT, CNT-g-PDDT/P3HT and rGO-g-PDDT/P3HT samples.

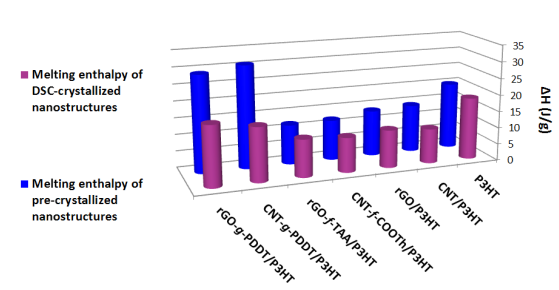

Fig. 7. Fusion enthalpy of melt- and solution-grown P3HT, CNT/P3HT, rGO/P3HT, CNT-f-COOTh/P3HT, rGO-f-TAA/P3HT, CNT-g-PDDT/P3HT and rGO-g-PDDT/P3HT nanostructures.

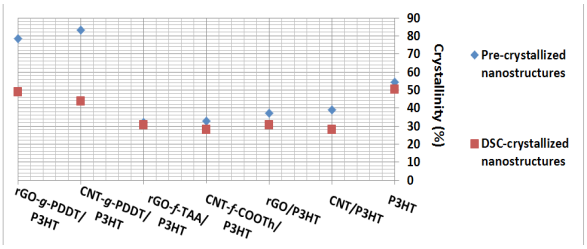

Fig. 8. Crystallinity (Xc) of pre-designed and DSC-crystallized P3HT, CNT/P3HT, rGO/P3HT, CNT-f-COOTh/P3HT, rGO-f-TAA/P3HT, CNT-g-PDDT/P3HT and rGO-g-PDDT/P3HT nano-hybrids.

4. CONCLUSION

Solution/melt-grown nanostructures were investigated on the basis of P3HT/carbonic materials from the structural, thermal, and optical perspectives. The functionalization and grafting of CNT and rGO precursors affected the sample characteristics. The crystallinity in the CNT-f-COOTh/P3HT and rGO-f-TAA/P3HT supramolecules was less than those detected in the CNT/P3HT and rGO/P3HT systems. In contrast, the –COOTh and –TAA functionalities did not influence the crystallization of host P3HTs in confined environments. More red-shifted absorbances, larger and more compact crystallites, and higher T_m, ΔH_m, and Xc values were recorded for the CNT-g-PDDT/P3HT stem-leaf (22.51 nm, 6.09 nm, 13.89 Å, 3.52 Å, 239.8 °C, 30.86 J/g and 83.40%) and rGO-g-PDDT/P3HT coarse-patched (20.76 nm, 5.96 nm, 13.95 Å, and 3.57 Å, 237.6 °C, 29.13 J/g and 78.73%) supramolecules. The quality of melt-grown CNT-g-PDDT/P3HT and rGO-g-PDDT/P3HT nanostructures was not as much as the respective stem-leaf and coarse-patched supramolecules, whereas they were better than the melt-grown CNT-f-COOTh/P3HT, CNT/P3HT, rGO-f-TAA/P3HT and rGO/P3HT samples.

CONFLICTS OF INTEREST

There are no conflicts of interest to declare.

REFERENCES

1. Willot, P., Steverlynck, J., Moerman, D., Leclère, P., Lazzaroni, R. and Koeckelberghs, G., "Poly (3-alkylthiophene) with Tuneable Regioregularity: Synthesis and Self-Assembling Properties. Polym". Chem., 2013, 4, 2662-2671.
2. Yazawa, K., Inoue, Y., Shimizu, T., Tansho, M. and Asakawa, N., "Molecular Dynamics of Regioregular Poly(3-hexylthiophene) Investigated by NMR Relaxation and An Interpretation of Temperature Dependent Optical Absorption". J. Phy. Chem. B, 2010, 114, 1241-1248.
3. Persson, N. E., Chu, P. H., McBride, M., Grover, M. and Reichmanis, E., "Nucleation, Growth, and Alignment of Poly(3-hexylthiophene) Nanofibers for High-Performance OFETs".Acc. Chem. Res.,2017, 50, 932-942.
4. Wadsworth, A., Hamid, Z., Bidwell, M., Ashraf, R. S., Khan, J. I., Anjum, D. H., Cendra, C., Yan, J., Rezasoltani, E., Guilbert, A. A. and Azzouzi, M., "Progress in Poly(3-hexylthiophene) Organic Solar Cells and the Influence of Its Molecular Weight on Device Performance". Adv. Energy Mater., 2018, 8, 1801001.
5. Seibers, Z. D., Le, T. P., Lee, Y., Gomez, E. D. and Kilbey, S. M., "Impact of Low Molecular Weight Poly (3-hexylthiophene) s as Additives in Organic Photovoltaic Devices". ACS Appl. Mater. Interfaces, 2018, 10, 2752-2761.
6. Rahimi, K., Botiz, I., Agumba, J. O., Motamen, S., Stingelin, N. and Reiter, G., "Light Absorption of Poly(3-hexylthiophene) Single Crystals". RSC Adv., 2014, 4, 11121-11123.
7. Zenoozi, S., Agbolaghi, S., Poormahdi, E., Hashemzadeh-Gargari, M. and Mahmoudi, M., "Verification of Scherrer Formula for Well-Shaped Poly(3-hexylthiophene)-Based Conductive Single Crystals and Nanofibers and Fabrication of Photovoltaic Devices from Thin Film Coating". Macromol. Res., 2017, 25, 826-840.

8. Zenoozi, S., Agbolaghi, S., Nazari, M. and Abbasi, F., "Thermal and Optical Properties of Nano/Micro Single Crystals and Nanofibers Obtained from Semiconductive-Dielectric Poly(3-hexylthiophene) Block Copolymers". Mat. Sci. Semicon. Proc., 2017, 64, 85-94.
9. Balko, J., Lohwasser, R. H., Sommer, M., Thelakkat, M. and Thurn-Albrecht, T., "Determination of the Crystallinity of Semicrystalline Poly(3-hexylthiophene) by Means of Wide-Angle X-ray Scattering". Macromolecules, 2013, 6, 9642-9651.
10. Snyder, C. R., Nieuwendaal, R. C., DeLongchamp, D. M., Luscombe, C. K., Sista, P. and Boyd, S. D., "Quantifying Crystallinity in High Molar Mass Poly(3-hexylthiophene)". Macromolecules, 2014, 47, 3942-3950.
11. Lee, C. S. and Dadmun, M. D., "Important Thermodynamic Characteristics of Poly(3-hexyl thiophene)". Polymer, 2014, 55, 4-7.
12. Liu, X. I., Ly, J., Han, S. O., Zhang, D. A., Requicha, A., Thompson, M. E. and Zhou, C. H., "Synthesis and Electronic Properties of Individual Single-Walled Carbon Nanotube/Polypyrrole Composite Nanocables". Adv. Mater., 2005, 17, 2727-2732.
13. Tchmutin, I. A., Ponomarenko, A. T., Krinichnaya, E. P., Kozub, G. I. and Efimov, O. N., "Electrical Properties of Composites Based on Conjugated Polymers and Conductive Fillers". Carbon, 2003, 41, 1391-1395.
14. Goh, R. G., Motta, N., Bell, J. M. and Waclawik, E. R., "Effects of Substrate Curvature on the Adsorption of Poly(3-hexylthiophene) on Single-Walled Carbon Nanotubes". Appl. Phys. Lett., 2006, 88, 053101.
15. Star, A., Stoddart, J. F., Steuerman, D., Diehl, M., Boukai, A., Wong, E. W., Yang, X., Chung, S. W., Choi, H. and Heath, J. R., "Preparation and Properties of Polymer-Wrapped Single-Walled Carbon Nanotubes". Angew. Chem., 2001, 113, 1771-1775.
16. Chen, J., Liu, H., Weimer, W. A., Halls, M. D., Waldeck, D. H. and Walker, G. C., "Noncovalent Engineering of Carbon Nanotube Surfaces by Rigid, Functional Conjugated Polymers". J. Am. Chem. Soc., 2002, 124, 9034-9035.
17. Lin, Y. H., Jiang, C., Xu, J., Lin, Z. and Tsukruk, V. V., "Robust Fluorescent and Nanoscale Freestanding Conjugated Films". Soft Matter, 2007, 3, 432-436.
18. Pal, S., Roy, S. and Nandi, A. K., "Temperature Variation of DC Conductivity of Poly(3-alkyl thiophenes) and Their Cocrystals". J. Phy. Chem. B, 2005, 109, 18332-18341.
19. Kobashi, M. and Takeuchi, H., "Inhomogeneity of Spin-Coated and Cast Non-Regioregular Poly(3-hexylthiophene) Films. Structures and Electrical and Photophysical Properties". Macromolecules, 1998, 31, 7273-7278.
20. Liu, J., Zou, J. and Zhai, L., "Bottom-up Assembly of Poly(3-hexylthiophene) on Carbon Nanotubes: 2D Building Blocks for Nanoscale Circuits". Macromol. Rapid Comm., 2009, 30, 1387-1391.
21. Liu, J., Moo-Young, J., McInnis, M., Pasquinelli, M. A. and Zhai, L., "Conjugated Polymer Assemblies on Carbon Nanotubes". Macromolecules, 2014, 47, 705-712.
22. Misra, R. D. K., Depan, D., Challa, V. S. A. and Shah, J. S., "Supramolecular Structures Fabricated Through the Epitaxial Growth of Semiconducting Poly(3-hexylthiophene) on Carbon Nanotubes as Building Blocks of Nanoscale Electronics". Phys. Chem. Chem. Phys., 2014, 16, 19122-19129.
23. Dias, Y. and Yerushalmi-Rozen, R., "Entropic Effects in Carbon Nanotubes-Templated Crystallization of Poly(3-alkyl thiophenes, P3HT, P3OT)". Polymer, 2013, 54, 6399-6405.
24. Boon, F., Desbief, S., Cutaia, L., Douhéret, O., Minoia, A., Ruelle, B., Clément, S., Coulembier, O., Cornil, J., Dubois, P. and Lazzaroni, R., "Synthesis and Characterization of Nanocomposites Based on Functional Regioregular Poly(3-hexylthiophene) and Multiwall Carbon Nanotubes". Macromol. Rapid Comm., 2010, 31, 1427-1434.
25. Challa, V. S. A., Nune, K. C. and Misra, R. D. K., "The Impact of Molecular Weight on Nanoscale Supramolecular Structure of Semiconducting Poly(3-hexylthiophene) on Carbon Nanotubes and Photophysical Properties". Mater. Technol., 2016, 31, 477-481.
26. Depan, D., Khattab, A., Simoneaux, A. and Chirdon, W., "Crystallization Kinetics of High-Density and Low-Density Polyethylene on Carbon Nanotubes. Polymer Crystallization", 2019, 2, e10062.
27. Chunder, A., Liu, J. and Zhai, L., "Reduced Graphene Oxide/Poly(3-hexylthiophene) Supramolecular Composites". Macromol. Rapid Comm., 2010, 31, 380-384.
28. Shrotriya, G., Li, V., Huang, J., Yao, Y., Moriarty, T., Emery, K. and Yang, Y., High-Efficiency Solution Processable Polymer Photovoltaic Cells by Self-Organization of Polymer Blends.

Nat. Mater., 2005, 4, 864-868.
29. Yang, Z. and Lu, H., "Nonisothermal Crystallization Behaviors of Poly(3-hexylthiophene)/ Reduced Graphene Oxide Nanocomposites". J. Appl. Polym. Sci., 2013, 128, 802-810.
30. Skrypnychuk, V., Boulanger, N., Yu, V., Hilke, M., Mannsfeld, S. C., Toney, M. F. and Barbero, D. R., "Enhanced Vertical Charge Transport in a Semiconducting P3HT Thin Film on Single Layer Graphene". Adv. Funct. Mater., 2015, 25, 664-670.
31. Kim, D. H., Lee, H. S., Shin, H. J., Bae, Y. S., Lee, K. H., Kim, S. W., Choi, D. and Choi, J. Y., "Graphene Surface Induced Specific Self-Assembly of Poly(3-hexylthiophene) for Nanohybrid Optoelectronics: From First-Principles Calculation to Experimental Characterizations". Soft Matter, 2013, 9, 5355-5360.
32. Zhou, X., Chen, Z., Qu, Y., Su, Q. and Yang, X., "Fabricating Graphene Oxide/Poly(3-butylthiophene) Hybrid Materials with Different Morphologies and Crystal Structures". RSC Adv., 2013, 3, 4254-4260.
33. Zhou, X. and Yang, X., "Improved Dispersibility of Graphene Oxide in o-Dichlorobenzene by Adding a Poly(3-alkylthiophene)". Carbon, 2012, 50, 4566-4572.
34. Lohwasser, R. H. and Thelakkat, M., "Toward Perfect Control of End Groups and Polydispersity in Poly(3-hexylthiophene) via Catalyst Transfer Polymerization". Macromolecules, 2011, 44, 3388-3397.
35. Agostinelli, T., Lilliu, S., Labram, J. G., Campoy-Quiles, M., Hampton, M., Pires, E., Rawle, J., Bikondoa, O., Bradley, D. D., Anthopoulos, T. D. and Nelson, J., "Real-Time Investigation of Crystallization and Phase-Segregation Dynamics in P3HT: PCBM Solar Cells During Thermal Annealing". Adv. Funct. Mater., 2011, 21, 1701-1708.
36. Bodor, G., Structural Investigation of Polymers, Ellis Horwood, Chichester, UK, 1991.
37. Kim, J. Y. and Frisbie, C. D., "Correlation of Phase Behavior and Charge Transport in Conjugated Polymer/Fullerene Blends". J. Phys. Chem. C, 2008, 112, 17726-17736.
38. Wu, Z., Petzold, A., Henze, T., Thurn-Albrecht, T., Lohwasser, R. H., Sommer, M. and Thelakkat, M., "Temperature and Molecular Weight Dependent Hierarchical Equilibrium Structures in Semiconducting Poly(3-hexylthiophene)". Macromolecules, 2010, 43, 4646-4653.
39. Pascui, O. F., Lohwasser, R., Sommer, M., Thelakkat, M., Thurn-Albrecht, T. and Saalwächter, K., "High Crystallinity and Nature of Crystal−Crystal Phase Transformations in Regioregular Poly(3-hexylthiophene)". Macromolecules, 2010, 43, 9401-9410.